Electronic Supplementary Material (ESI) for ChemComm.

Supporting Information

Yet again, new compounds found in systems with known binary phase diagrams. Synthesis, crystal and electronic structure of Nd_3Bi_7 and Sm_3Bi_7

Alexander Ovchinnikov, Julien P. A. Makongo and Svilen Bobev

Department of Chemistry and Biochemistry, University of Delaware,

Newark, Delaware 19716, United States

Contents:

1. Synthesis details

All operations except heat treatment were performed inside an argon-filled glovebox with oxygen and water contents below 0.1 ppm and 0.5 ppm, respectively.

1.1. Powder samples

Single phase powder samples of Nd_3Bi_7 and Sm_3Bi_7 were prepared by a direct combination of elements (Alfa, all with purity >99.9 wt. %). First, small pieces of the rare-earth metal and Bi were mixed in the stoichiometric ratio and placed in an alumina crucible sealed inside an evacuated fused silica tube. The total mass of the pellet was 500 mg. The reaction mixture was annealed at 450 ^{o}C for four days. After that, the resulting solid product was finely ground and pelletized. The pellet was annealed for additional two weeks at the same temperature.

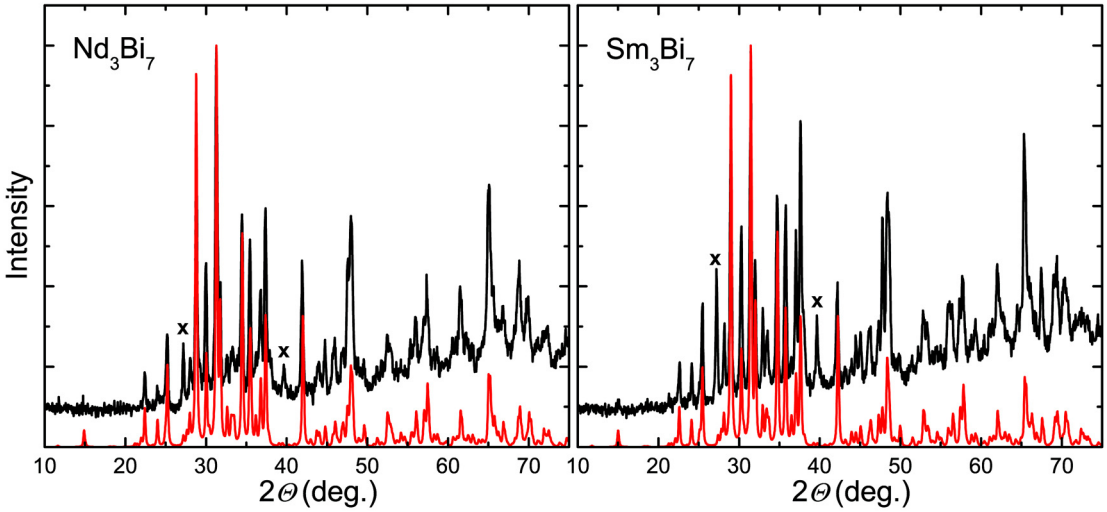

Figure S1. Experimental (black) and theoretical (red) PXRD patterns for RE_3Bi_7 (*RE* = Nd, Sm). Crosses mark the positions of the most intense Bragg peaks of the elemental Bi.

Powder X-ray diffraction patterns were collected on a Rigaku Miniflex diffractometer (Cu K_α radiation, λ = 1.5418 Å) in a Θ–Θ mode between 10^{o} and 75^{o} with a step size of 0.05^{o} and 2 s/step counting time. Theoretical patterns were generated using the structural parameters obtained from the refinement of the single-crystal X-ray diffraction data.

The synthetic procedure described above yielded almost single-phase samples of RE_3Bi_7 (*RE* = Nd, Sm) as indicated by PXRD analysis (Figure S1). The only observed impurity was the elemental Bi that must have formed on the grain boundaries upon short exposure of the

finely ground powders to air. Attempts were undertaken to obtain the RE_3Bi_7 phases for *RE* = La–Pr, Eu and Gd using the same synthetic protocol, but these reactions failed to yield the desired products. The reaction outcomes are given in Table S1.

Table S1. Products of the reaction 3×*RE* + 7×Bi (450 °C, 18 days with an intermediate regrinding) for *RE* = La–Pr, Eu and Gd

RE	Products
La	$LaBi_2$, Bi
Ce	$CeBi_2$, Bi
Pr	$PrBi_2$, Bi
Eu	$EuBi_2$, $EuBi_3$
Gd	GdBi, Bi

1.2. Single crystal growth procedure

For the single-crystal growth of Nd_3Bi_7 and Sm_3Bi_7, the corresponding rare-earth metals (*RE*) were mixed with Bi in the ratio *RE* : Bi = 1 : 100. The mixture (total mass of ca. 3 g) was placed in an alumina crucible and topped with a piece of quartz wool acting as a filter. The crucible was enclosed in an evacuated fused silica tube and heated up to 1000 °C with 200 °C/h. After homogenization at this temperature for 5 h, the mixture was cooled down to 700 °C with 50 °C/h, and then to 400 °C with 5 °C/h. At this temperature, the reaction tube was taken out from the furnace, flipped over, and the excess of molten Bi was removed by centrifugation.

The large excess of Bi in comparison with the stoichiometric composition was necessary to assure complete dissolution of the rare-earth metal and to prevent the formation of the binary bismuthides $REBi_2$. The liquidus line for the latter apparently extends to high Bi concentrations, resulting in the precipitation of these undesired binary phases even from rather Bi-rich compositions, e.g. *RE* : Bi = 1 : 20.

The reaction tubes were crack-opened inside the glovebox. Single crystals of RE_3Bi_7 (*RE* = Nd, Sm) were the only product observed in the alumina crucible and on the quartz wool filter. Both Nd_3Bi_7 and Sm_3Bi_7 grow with a needle-like morphology. Smaller needles tend to form agglomerates, whereas larger needles with linear dimensions up to 4 mm appear as individual single crystals upon inspection under an optical microscope. PXRD patterns of the ground crystals were consistent with those of the powder samples produced at 450 °C.

2. Single-crystal X-ray diffraction (SCXRD)

Single-crystals suitable for X-ray diffraction were cut in dry Paratone-N oil from individual flux-grown needles. Data collection was done at T = 200 K on a Bruker SMART CCD-diffractometer equipped with monochromated Mo K_α radiation (λ = 0.71073 Å). The raw data were integrated using the program SAINT.[1] Semiempirical absorption corrections were applied with the SADABS software.[2] Crystal structures were solved by direct methods and refined by full matrix least-squares methods on F^2 using SHELXL.[3] Generating of the initial model in space group *Immm* (No. 71) and further refinements were straightforward. All atoms were refined anisotropically. The largest residual electron density peaks were located in the vicinity of the heavy Bi atoms—an apparent artifact of the semi-empirical absorption corrections (N.B. the absorption coefficients are extremely high, exceeding 1000 cm^{-1}).

Table S2. Data collection details and selected crystallographic data for RE_3Bi_7 (*RE* = Nd, Sm; space group *Immm*, Z = 4, T = 200 K, Mo K_α λ = 0.71073 Å)

Refined composition	Nd_3Bi_7	Sm_3Bi_7
Molecular weight/ g mol^{-1}	1895.58	1913.91
a/ Å	4.2996(6)	4.2762(8)
b/ Å	15.200(2)	15.050(3)
c/ Å	19.121(3)	19.034(4)
V/ $Å^3$	1249.6(3)	1225.0(4)
ρ_{calc}/ g cm^{-3}	10.076	10.378
$\mu_{MoK\alpha}$/ cm^{-1}	1103.4	1142.2
R_1 [$I > 2\sigma(I)$][a]	0.040	0.043
wR_2 [$I > 2\sigma(I)$][a]	0.082	0.086
R_1 [all data][a]	0.056	0.058
wR_2 [all data][a]	0.089	0.092
$\Delta\rho_{max,min}$/ e $Å^{-3}$	3.21, –3.89	3.04, –4.51

[a]$R1 = \sum||F_o|-|F_c||/\sum|F_o|$; $wR_2 = [\sum[w(F_o^2-F_c^2)^2]/\sum[w(F_o^2)^2]]^{1/2}$, where $w = 1/[\sigma^2F_o^2+(0.0248P)^2]$ for Nd_3Bi_7, and $w = 1/[\sigma^2F_o^2+(0.0221P)^2]$ for Sm_3Bi_7. $P = (F_o^2+2F_c^2)/3$; CIFs have been deposited with reference numbers CCDC 1833009 for Nd_3Bi_7, and CCDC 1833010 for Sm_3Bi_7.

Table S3. Atomic coordinates and equivalent isotropic displacement parameters (Å^2) for Nd_3Bi_7

Atom	Site	*x*	*y*	*z*	U_{eq}[a]
Nd1	8*l*	0	0.13913(7)	0.36829(6)	0.0158(2)
Nd2	4*i*	0	0	0.17266(8)	0.0160(3)
Bi1	8*l*	0	0.21176(5)	0.19682(4)	0.0170(2)
Bi2	8*l*	0	0.36019(5)	0.41198(4)	0.0190(2)
Bi3	4*j*	1/2	0	0.30090(6)	0.0164(2)
Bi4	4*g*	0	0.33521(7)	0	0.0179(2)
Bi5	2*c*	1/2	1/2	0	0.0191(3)
Bi6	2*a*	0	0	0	0.0213(3)

[a]U_{eq} is defined as one third of the trace of the orthogonalized U_{ij} tensor.

Table S4. Anisotropic displacement parameters (Å^2) for Nd_3Bi_7

Atom	U_{11}	U_{22}	U_{33}	U_{12}	U_{13}	U_{23}
Nd1	0.0153(5)	0.0173(5)	0.0148(5)	0	0	0.0009(4)
Nd2	0.0173(8)	0.0162(6)	0.0144(7)	0	0	0
Bi1	0.0171(4)	0.0175(3)	0.0163(4)	0	0	0.0001(3)
Bi2	0.0189(4)	0.0200(4)	0.0182(4)	0	0	–0.0004(3)
Bi3	0.0151(5)	0.0179(5)	0.0162(5)	0	0	0
Bi4	0.0165(5)	0.0230(5)	0.0142(5)	0	0	0
Bi5	0.0248(9)	0.0184(7)	0.0139(7)	0	0	0
Bi6	0.0192(8)	0.0288(8)	0.0158(7)	0	0	0

Table S5. Atomic coordinates and equivalent isotropic displacement parameters (Å^2) for Sm_3Bi_7

Atom	Site	*x*	*y*	*z*	U_{eq}[a]
Sm1	8*l*	0	0.13886(8)	0.36812(8)	0.0156(3)
Sm2	4*i*	0	0	0.1731(1)	0.0145(4)
Bi1	8*l*	0	0.21180(6)	0.19686(5)	0.0154(3)
Bi2	8*l*	0	0.36056(6)	0.41167(6)	0.0179(3)
Bi3	4*j*	1/2	0	0.30095(7)	0.0152(3)
Bi4	4*g*	0	0.33396(9)	0	0.0170(3)
Bi5	2*c*	1/2	1/2	0	0.0168(4)
Bi6	2*a*	0	0	0	0.0195(4)

[a]U_{eq} is defined as one third of the trace of the orthogonalized U_{ij} tensor.

Table S6. Anisotropic displacement parameters (Å^2) for Sm_3Bi_7

Atom	U_{11}	U_{22}	U_{33}	U_{12}	U_{13}	U_{23}
Sm1	0.0169(6)	0.0121(6)	0.0179(7)	0	0	0.0008(5)
Sm2	0.0173(9)	0.0119(8)	0.015(1)	0	0	0
Bi1	0.0174(5)	0.0124(5)	0.0166(5)	0	0	0.0004(3)
Bi2	0.0192(5)	0.0152(5)	0.0193(6)	0	0	–0.0001(4)
Bi3	0.0155(6)	0.0138(6)	0.0162(7)	0	0	0
Bi4	0.0157(7)	0.0189(7)	0.0163(8)	0	0	0
Bi5	0.023(1)	0.0141(9)	0.014(1)	0	0	0
Bi6	0.021(1)	0.023(1)	0.014(1)	0	0	0

Table S7. Selected interatomic distances (Å) in RE_3Bi_7 (*RE* = Nd, Sm)

Atoms	Nd	Sm
*RE*1—Bi3 × 2	3.2793(9)	3.252(1)
*RE*1—Bi5	3.289(1)	3.266(1)
*RE*1—Bi4 × 2	3.3341(9)	3.323(1)
*RE*1—Bi1 × 2	3.363(1)	3.340(1)
*RE*1—Bi1	3.460(1)	3.438(2)
*RE*1—Bi2	3.463(1)	3.440(2)
*RE*2—Bi1 × 2	3.2517(9)	3.220(1)
*RE*2—Bi3 × 2	3.261(2)	3.239(2)
*RE*2—Bi6	3.301(2)	3.295(2)
*RE*2—Bi2 × 4	3.429(1)	3.403(1)
Bi1—Bi1 × 2	3.180(1)	3.160(2)
Bi1—Bi2 × 2	3.1851(9)	3.166(1)
Bi2—Bi2	3.366(2)	3.363(2)
Bi2—Bi6 × 2	3.4597(7)	3.4354(9)
Bi4—Bi5 × 2	3.3009(9)	3.289(1)

3. Differential scanning calorimetry (DSC)

Simultaneous differential scanning calorimetry thermogravimetric (DSC/TG) analysis was carried out using a SDT Q600 analyzer, supplied by TA Instruments, under a constant flow of high-purity argon (100 ml/min). Polycrystalline RE_3Bi_7 intergrowths (*RE* = Nd, Sm) produced by the Bi flux method were loaded in capped alumina pans. After equilibration at 100 °C, the temperature was raised to 700 °C with 10 °C/min, kept at this point for 1 min, and lowered to 100 °C with 10 °C/min. The results of the DSC/TG measurements are shown in Figure S2. No significant mass changes were observed in any of the runs.

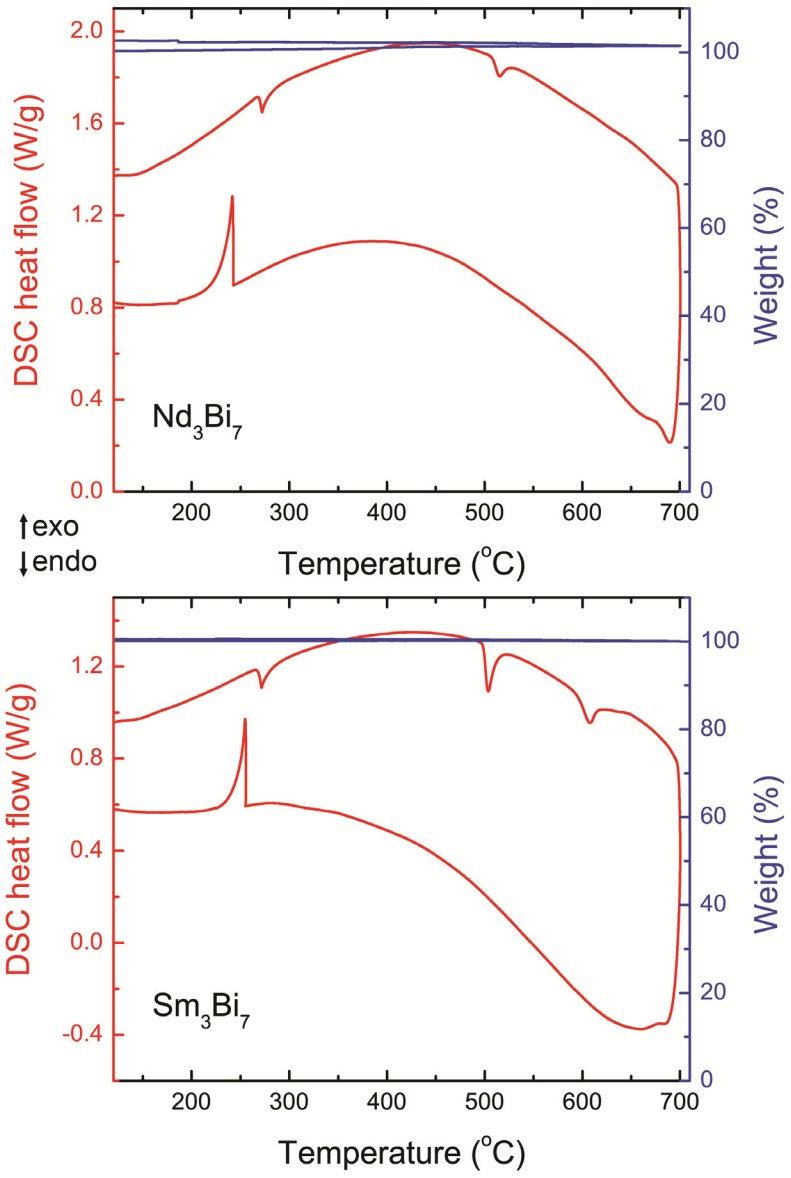

Figure S2. Results from the DSC/TG analysis for Nd_3Bi_7 (top) and Sm_3Bi_7 (bottom).

In both samples, a small endothermic peak is visible around 270 °C upon heating, indicating the melting of the residual Bi flux trapped between the individual crystals.

For Nd_3Bi_7, one intrinsic endothermic effect is observed upon heating at 508 °C. In the case of Sm_3Bi_7, two endothermic peaks are visible in the heating curve at 499 °C and 594 °C. PXRD analysis of the RE_3Bi_7 (*RE* = Nd, Sm) samples annealed at 650 °C for 30 min and air-quenched to room temperature revealed the presence of *RE*Bi and elemental Bi along with another product (Figure S3). The latter can be identified as $REBi_2$, although, since no structural data are available for the $NdBi_2$ and $SmBi_2$ phases, only a rough match with the reported Bragg peak positions was possible.[4,5]

Annealing of the Sm_3Bi_7 sample at 520 °C yielded a powder pattern similar to that obtained after annealing at 650 °C. Thus, the nature of the second endothermic event at 594 °C remains unclear. The decomposition of Sm_3Bi_7 with the onset temperature of 499 °C likely proceeds through an intermediate amorphous phase, which itself undergoes an endothermic transformation at 594 °C.

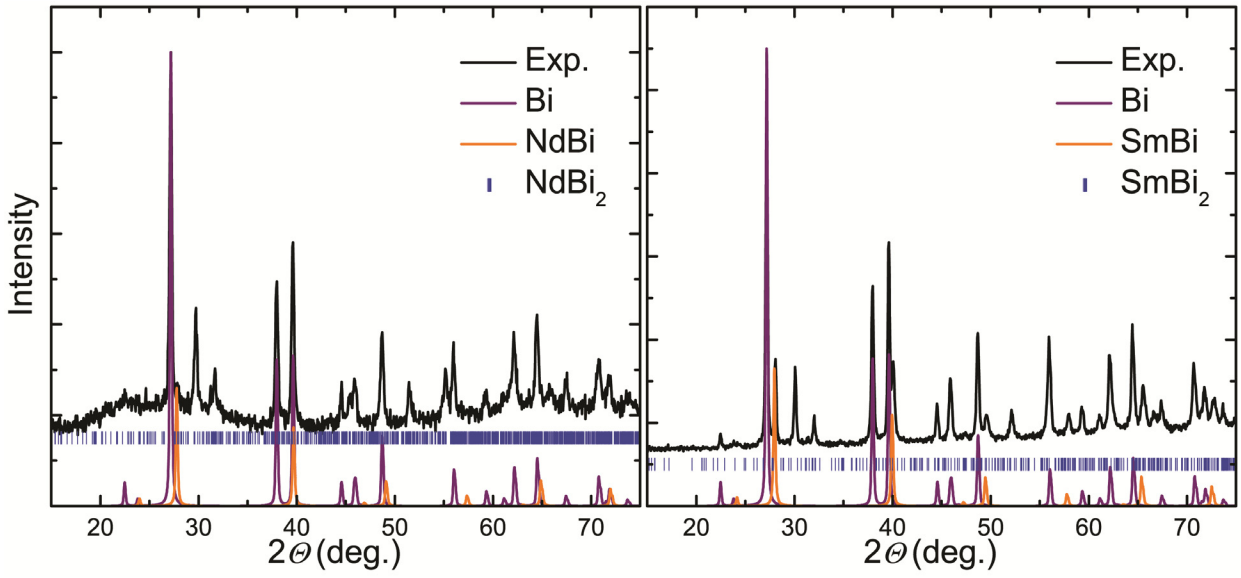

Figure S3. PXRD patterns of decomposition products (650 °C, 30 min) of Nd_3Bi_7 (left) and Sm_3Bi_7 (right).

Interestingly, dwelling of the decomposition products at 650 °C for five days does not result in significant changes of the PXRD patterns. According to the available phase diagrams,[5–7] for the composition *RE* : Bi = 3 : 7 at this temperature, the $REBi_2$ phases are expected to be in equilibrium with liquid Bi. Apparently, a high stability of the equiatomic *RE*Bi cubic phases,

which form upon decomposition of RE_3Bi_7, prohibits further transformation to $REBi_2$ despite the presence of the excessive Bi metal.

The cooling DSC curves display the solidification of Bi as the only thermal event. PXRD patterns of the slowly cooled DSC samples are identical to those of the air-quenched products. Although the back-formation of RE_3Bi_7 does not occur within the timeframe of the DSC experiment, annealing of the decomposition products at 450 ^{o}C for four days recovers the RE_3Bi_7 phases, suggesting that these compounds are thermodynamically stable at this temperature.

4. Physical property measurements

Temperature dependent electrical resistivity was measured from 5 to 300 K with an excitation current of 10 mA using a Quantum Design Physical Property Measurement System (PPMS). Four platinum wires were connected to single crystals of RE_3Bi_7 (*RE* = Nd, Sm) using EPO TEK H20E silver epoxy. The measurements were carried out on both heating and cooling for two different crystals to ensure reproducibility. Field-cooled direct current magnetization was measured on a collection of hand-picked single crystals using the PPMS in the temperature range T = 5–300 K under an applied field of 5000 Oe. The measurements were done for two different batches to ensure reproducibility.

5. First-principle calculations

Electronic structure calculations were performed for Nd_3Bi_7 with the SIESTA code[8] employing the LSDA+U approach to take into account strong correlations on the Nd 4f-orbitals. The rotationally invariant scheme was applied with U_{eff} = 4.0 eV, which is a typical value for rare-earth elements.[9] The Brillouin zone was sampled by a 6x6x6 k-point grid and the Perdew-Zunger variant of the exchange-correlation functional was used. The mesh cutoff was set to 200 Ry after checking for convergence. For simplicity, we only considered a ferro-magnetically ordered structure.

In addition, we conducted first-principle calculations for the hypothetical nonmagnetic compound La_3Bi_7. The initial structure was generated by extrapolating the unit cell parameters of RE_3Bi_7 (*RE* = Nd, Sm) for RE = La, while keeping the atomic coordinates of Nd_3Bi_7. At the next stage, the unit cell vectors and atomic coordinates were relaxed using the

Broyden–Fletcher–Goldfarb–Shanno (BFGS) algorithm implemented in the Quantum Espresso package.[10] The Perdew-Burke-Ernzerhof (PBE) flavor of the exchange-correlation functional was applied and the Brillouin zone was sampled by a 4×4×4 *k*-point grid. Kinetic energy cutoff for wavefunctions was set to 100 Ry after checking for convergence. The forces were converged to less than 0.003 Ry/a.u.

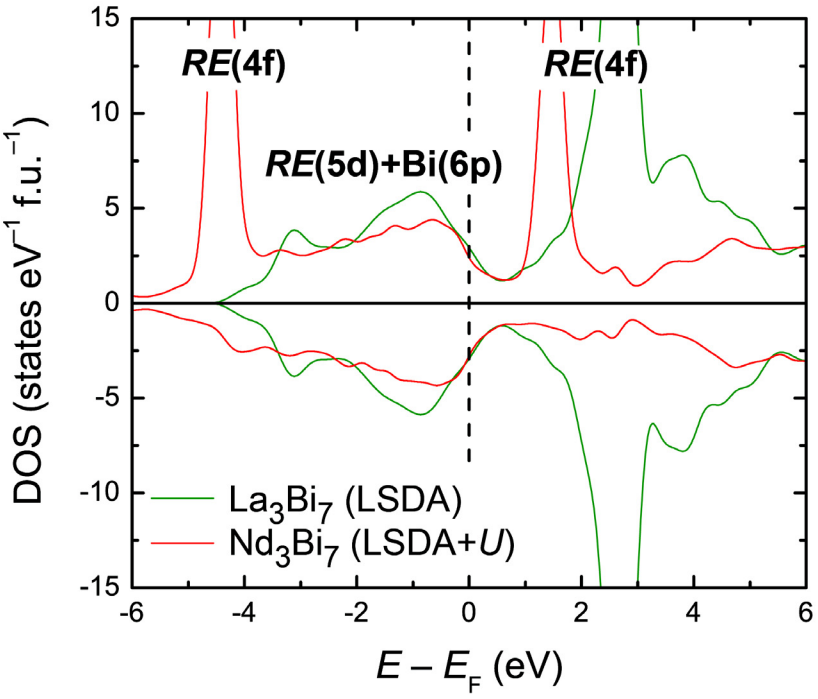

Figure S4. Electronic density of states (DOS) for Nd_3Bi_7 and La_3Bi_7. Positive and negative values correspond to majority and minority spin directions, respectively. Main contributions to the DOS are indicated (see the main text for details).

Aside from the differences in the 4f-states distribution arising from the magnetism in Nd_3Bi_7, the overall appearance of the electronic densities of states (Figure S4) is very similar for the two bismuthides. Since detailed analysis of the Nd_3Bi_7 electronic structure requires establishing the magnetic ground state, we continue discussion of the electron counting and chemical bonding for the nonmagnetic La_3Bi_7.

Table S8. Atomic coordinates of the optimized La_3Bi_7 structure (*Immm*, *a* = 4.4848 Å, *b* = 15.7190 Å, *c* = 19.2754 Å)

Atom	Site	*x*	*y*	*z*
La1	8*l*	0	0.13812	0.36784
La2	4*i*	0	0	0.17306
Bi1	8*l*	0	0.21351	0.19658
Bi2	8*l*	0	0.35920	0.41354
Bi3	4*j*	1/2	0	0.30123
Bi4	4*g*	0	0.34295	0
Bi5	2*c*	1/2	1/2	0
Bi6	2*a*	0	0	0

The optimized La_3Bi_7 structure (Table S8) was used as an input for the all-electron TB-LMTO-ASA code.[11] For the latter, the von-Barth-Hedin functional was employed and a 16×16×16 *k*-point grid was used to sample the Brillouin zone. To satisfy the atomic sphere approximation (ASA), an introduction of empty spheres was necessary. Chemical bonding was interrogated using the Crystal Orbital Hamilton Population (COHP) analysis.

The electronic band structure for La_3Bi_7 is shown in Figure S5. The bands in the vicinity of the Fermi level (E_F) have mainly La(5d) and Bi(6p) character. Above the Fermi level, a dense manifold of the La(4f) states is located, resulting in a peak in the density of states (Figure 2 in the main text). Localized bands below circa $E - E_F = -8.0$ eV stem from the Bi(6s) states and hallmark the lone pair effect.

The COHP and integrated COHP (ICOHP) curves for selected symmetrically independent interactions are displayed in Figure S6. The pattern of interconnecting Bi atoms forming the anionic subunits in RE_3Bi_7 is shown in Figure S7 for reference.

The La–Bi interactions in La_3Bi_7 show bonding character below the Fermi level. Small peaks of bonding states also extend above E_F, making these interactions slightly underoptimized. A band of unoccupied antibonding states is located at $E - E_F > 1.8$ eV.

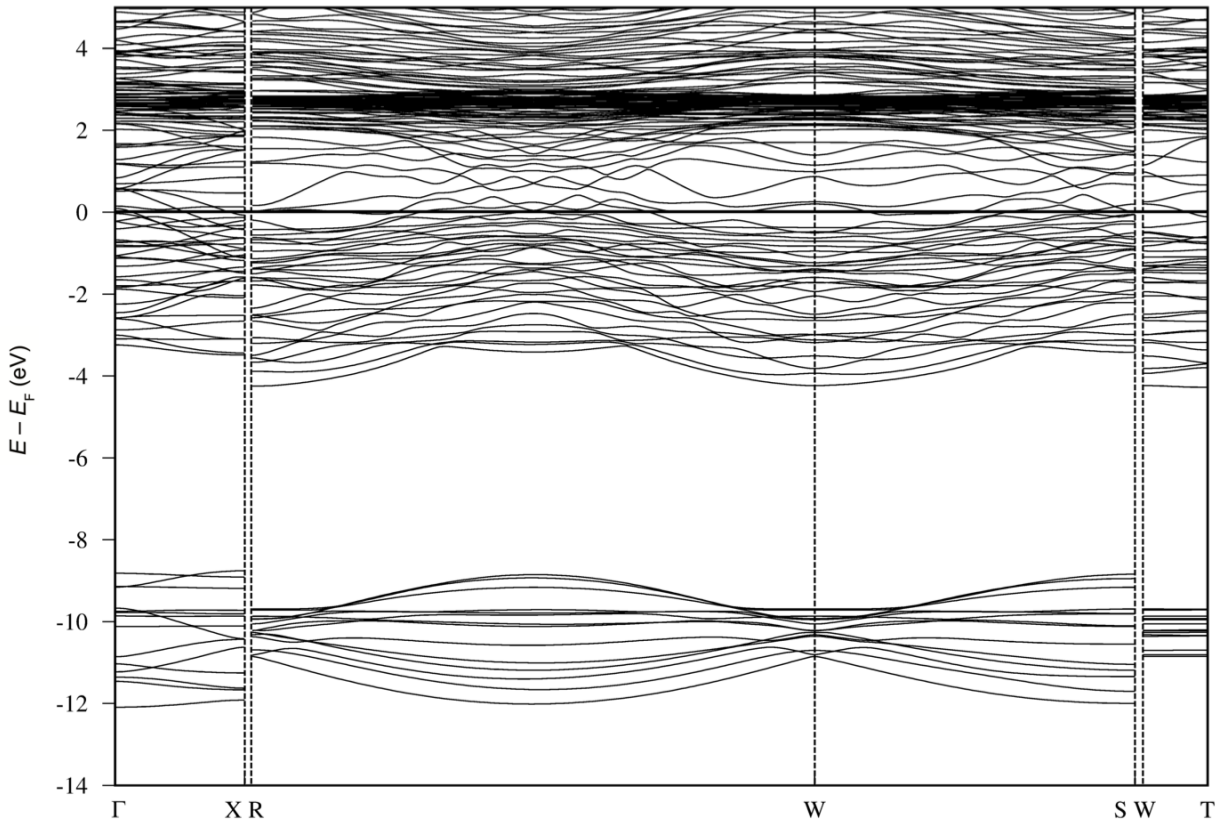

Figure S5. Electronic band structure along selected directions for the hypothetical La_3Bi_7 compound.

All Bi–Bi contacts show a combination of low-lying bonding states and smaller peaks of antibonding character located just below the Fermi level. Such a pattern of electronic state distribution along with the overall underoptimized bonding interaction is typical for hypervalent *Pn*–*Pn* bonds.[12,13] Indeed, the interatomic Bi–Bi distances in the optimized La_3Bi_7 structure, as well as in RE_3Bi_7 (*RE* = Nd, Sm), appear to be longer than single Bi–Bi bonds, but fall in the range of bonding contacts in electron-rich (hypervalent) bismuthides.[14–15] The –ICOHP values for the individual Bi–Bi interactions range from about 0.4 to 0.8 eV/bond. Taken as a measure of the strength of chemical interactions, these values expectedly increase with decreasing Bi–Bi interatomic separation. It is therefore reasonable to assume that for RE_3Bi_7 (*RE* = Nd, Sm), the contribution of the Bi–Bi interactions to the stability of the structure will be more substantial due to the shorter Bi–Bi bonds, whereas for earlier rare-earth metals, the large size of the *RE* cation leads to the expansion of the unit cell and weakening of the hypervalent bonding.

For the Bi1–Bi1 and Bi2–Bi2 interactions, the Fermi level crosses broad peaks of antibonding character, indicating possible electronic instability. Raising the electron count by about two electrons per formula unit will shift the Fermi level to a hollow in the density of states located ≈ 0.5 eV above the original E_F and to the base of the antibonding peaks. Besides lifting the electronic instability, such electron doping results in population of the bonding La–Bi states, although at the expense of the Bi–Bi interactions. The latter, being already electron-rich, suffer from further underoptimization when the number of electrons increases. Such an unfavorable effect can be counterbalanced by additional bonding interaction, as in the case of $RE_6Zn_{1+x}Sb_{14}$ (*RE* = Sm, Gd–Ho)[16] and Ce_6ZnBi_{14},[17] representing stuffed variants of the $(U_{0.5}Ho_{0.5})_3Sb_7$ structure. These compounds appear to be stabilized by additional Zn–*Pn* (*Pn* = Sb, Bi) interactions, whereas the binary phases Ce_6Bi_{14} (≡ Ce_3Bi_7) and RE_6Sb_{14} (≡ RE_3Sb_7; *RE* = Sm, Gd–Ho) are not known. The idealized composition $RE_6Zn_2Pn_{14}$ (≡ RE_3ZnPn_7) corresponds to exactly two extra electrons added to the RE_3Pn_7 formula unit. In line with our calculations, which predict shifting of the Fermi level to a minimum in the DOS, the hypothetical $Gd_6Zn_2Sb_{14}$ displays a pseudogap at the Fermi level.[16]

Similarly, the prototypic $(U_{0.5}Ho_{0.5})_3Sb_7$, reportedly containing U^{4+},[18] possesses 1.5 extra electrons per formula unit in comparison with the hypothetical Ho_3Sb_7, with additional stabilization coming presumably from shorter *RE*–Sb bonds (*RE* = U/Ho). Thus, Nd_3Bi_7 and Sm_3Bi_7 appear so far to be the only truly binary compounds of the $(U_{0.5}Ho_{0.5})_3Sb_7$ structure type stable without electron doping.

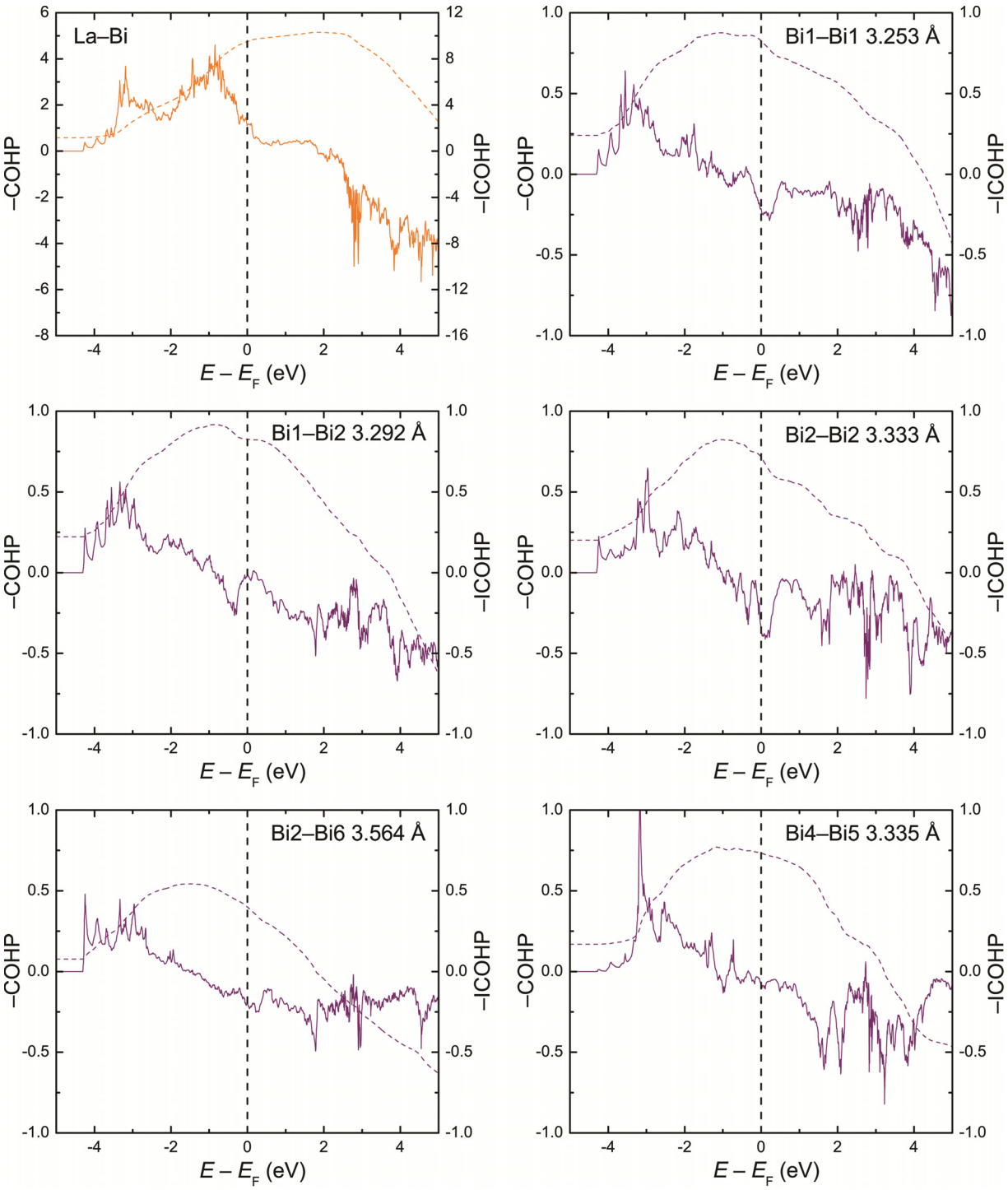

Figure S6. COHP curves for selected interatomic contacts in La_3Bi_7.

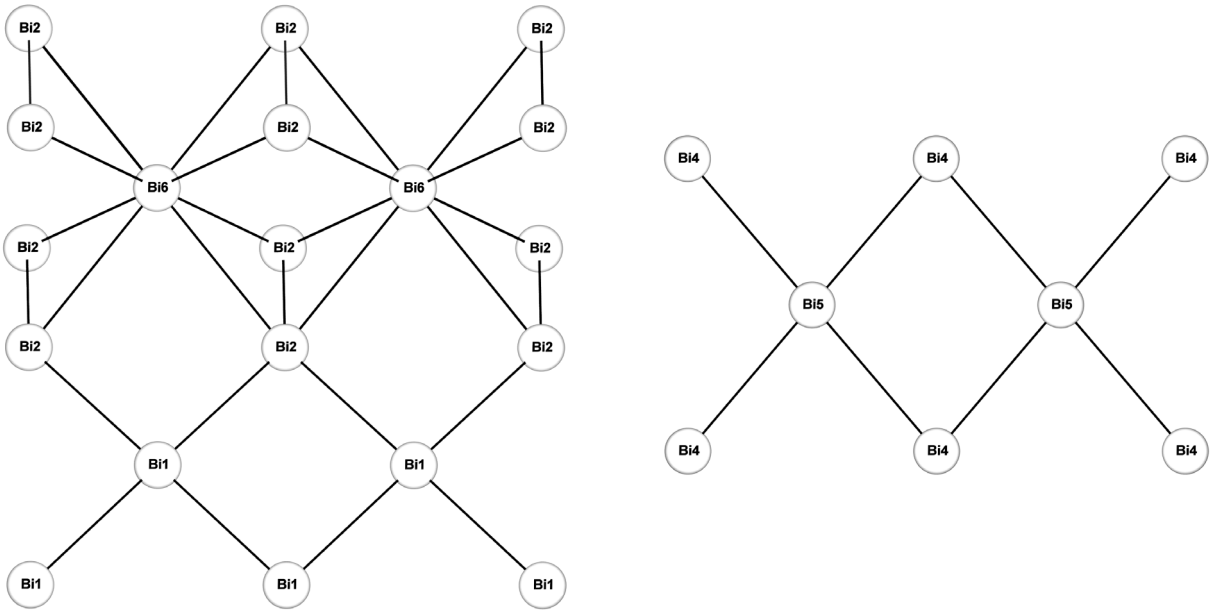

Figure S7. Labeling of the Bi atoms in the anionic subunits of RE_3Bi_7.

6. References

1 *SAINT; Bruker AXS Inc., Madison, Wisconsin, USA, 2014*.
2 *SADABS; Bruker AXS Inc., Madison, Wisconsin, USA, 2014*.
3 G. M. Sheldrick, *Acta Crystallogr. Sect. C Struct. Chem.*, 2015, **71**, 3–8.
4 K. Yoshihara, J. B. Taylor, L. D. Calvert and J. G. Despault, *J. Common Met.*, 1975, **41**, 329–337.
5 F. M. Sadigov, O. M. Aliyev and P. G. Rustamov, *J. Common Met.*, 1985, **113**, 17–19.
6 K. A. Gschneidner jr. and F. W. Calderwood, *Bull. Alloy Phase Diagr.*, 1989, **10**, 444–446.
7 V. D. Abulkhaev, *Russ. J. Inorg. Chem.*, 2001, **46**, 580–583.
8 J. M. Soler, E. Artacho, J. Gale, A. García, J. Junquera, P. Ordejón and D. Sánchez-Portal, *J. Phys.: Condens. Mater* 2002, **14**, 2745–2779.
9 A. Aburto and E. Orgaz, *Phys. Rev. B* 2007, **75**, 045130.
10 P. Giannozzi, S. Baroni, N. Bonini, M. Calandra, R. Car, C. Cavazzoni, D. Ceresoli, G. L. Chiarotti, M. Cococcioni, I. Dabo, A. Dal Corso, S. de Gironcoli, S. Fabris, G. Fratesi, R. Gebauer, U. Gerstmann, C. Gougoussis, A. Kokalj, M. Lazzeri, L. Martin-Samos, N. Marzari, F. Mauri, R. Mazzarello, S. Paolini, A. Pasquarello, L. Paulatto, C. Sbraccia, S. Scandolo, G. Sclauzero, A. P. Seitsonen, A. Smogunov, P. Umari and R. M. Wentzcovitch, *J. Phys. Condens. Matter*, 2009, **21**, 395502.
11 O. Jepsen and O. K. Andersen, *The Stuttgart TB-LMTO-ASA Program, Version 4.7; Max-Planck-Institut für Festkörperforschung: Stuttgart, Germany*, .
12 G. A. Papoian and R. Hoffmann, *Angew. Chem. Int. Ed.*, 2000, **39**, 2408–2448.
13 A. Ovchinnikov and S. Bobev, *Acta Crystallogr. Sect. C Struct. Chem.*, 2018, **74**, 269–273.
14 T. Y. Kuromoto, S. M. Kauzlarich and D. J. Webb, *Chem. Mater.*, 1992, **4**, 435–440.
15 A. Ovchinnikov, B. Saparov, S.-Q. Xia and S. Bobev, *Inorg. Chem.*, 2017, **56**, 12369–12378.
16 Y. Liu, L. Chen, L.-H. Li, L.-M. Wu, O. Y. Zelinska and A. Mar, *Inorg. Chem.*, 2008, **47**, 11930–11941.
17 A. V. Tkachuk, T. Tam and A. Mar, *Chem. Met. Alloys*, 2008, **1**, 76–83.
18 T. Schmidt and W. Jeitschko, *Inorg. Chem.*, 2001, **40**, 6356–6361.